

Laboratory Studies of Cosmology Inspired Defect Dynamics in Liquid Crystals

Semester Long Project Report

Anik Mandal^{1,*}

SLP Guide : Prof. Pramoda Kumar¹

SLP Mentor : Ankit Gupta¹

PhD Supervisor : Prof. Somak Raychaudhury¹

¹Ashoka University, Sonipat, India

*Email: anik.mandal_phd24@ashoka.edu.in



January 11, 2026

Abstract

Spontaneous symmetry breaking in the early universe is expected to generate topological defects whose dynamics encode high-energy physics beyond the reach of terrestrial accelerators, a phenomenon modeled here using nematic liquid crystals to test the Kibble–Zurek mechanism (KZM) and one-scale coarsening models. In this work, a homeotropically aligned MBBA cell was driven across the Fréedericksz transition using controlled AC electric fields, while high-speed optical microscopy recorded defect formation and evolution. A dedicated computational framework was developed to extract defect line density as a function of time and control parameters. For late-time dynamics in a cell with pre-existing defects, the defect density exhibits a power-law decay $\rho(t) \propto t^{-1}$ within uncertainties, consistent with string-dominated one-scale coarsening, whereas a newly prepared, defect-free cell initially forms closed-loop structures with substantially slower effective exponents, reflecting a crossover from loop-dominated to line-dominated regimes. Attempts to probe KZ scaling in defect formation using high-frequency (10 kHz) sawtooth field ramps revealed a freeze-out of director dynamics and strong stochasticity, while lowering the frequency led to electroconvection; these results delineate the practical parameter space for cosmology-inspired experiments in nematic liquid crystals, highlighting the robustness of late-time coarsening scaling while identifying specific challenges in accessing defect-formation scaling in electrically driven MBBA cells.

Contents

1	Introduction	2
1.1	Symmetry-breaking in early Universe	2
1.2	Kibble-Zurek mechanism	5
1.3	Project objectives	8
2	Experimental Setup	9
2.1	Preparing empty cell	9
2.2	Capacitance-based cell thickness measurement	10
2.3	Preparing homeotropic cell	11
2.4	Optical microscopy system	11
3	Computational Framework	12
3.1	Pre-processing and noise reduction	12
3.2	Ridge detection operation	12
3.3	Calculating defect density	13
4	Defect Dynamics	15
4.1	The Fréedericksz transition	15
4.2	Late-time coarsening dynamics	16
4.3	Defect formation dynamics	19
4.4	Error analysis	20
5	Conclusion	23
A	Acknowledgements	24
B	Late-time coarsening	26

1 Introduction

Spontaneous symmetry breaking is a fundamental phenomenon where the lowest energy state (ground state) of a system exhibits less symmetry than the physical laws governing it. At high temperatures or energy levels, the system exists in a symmetric, disordered state. However, as the system cools below a critical threshold, it becomes energetically favorable to transition to an ordered state. To do so, the system must spontaneously select a specific orientation from a set of equally valid possibilities.

A classic analogy is a ball sitting at the peak of a “Mexican hat” potential: while the shape of the potential itself is perfectly symmetric, the ball must eventually roll down into the valley to minimize its energy. In doing so, it chooses a random direction, thereby breaking the rotational symmetry. In the context of both cosmology and condensed matter physics, this choice happens independently in different regions of space. When these disparate regions eventually meet, their orientations often fail to align smoothly, leading to the formation of stable discontinuities known as topological defects [1].

1.1 Symmetry-breaking in early Universe

Current cosmological models indicate that during the Planck epoch and the earliest high-energy stages of cosmic evolution, all fundamental interactions were unified into a single force. At these extreme energy scales, the Universe existed in a maximally symmetric state in which the distinctions between the strong, weak, and electromagnetic interactions were absent. As the universe expanded and cooled below a series of critical temperatures, it underwent successive phase transitions driven by spontaneous symmetry breaking [2, 3]. These transitions are not merely abstract mathematical constructs; rather, they play a fundamental role in reshaping the vacuum state of the universe. In this sense, they are closely analogous to phase transitions in condensed matter systems, such as the freezing of water into ice or the emergence of ferromagnetic order.

In particle physics, the unification of weak and electromagnetic interactions into an electroweak gauge theory based on $SU(2) \times U(1)$ is well established. Together with Quantum Chromodynamics (QCD), the $SU(3)$ theory of strong interactions, this naturally motivates Grand Unified Theories (GUTs), in which the Standard Model forces are embedded within a larger simple gauge group, G . This unification is possible because the strengths of the fundamental forces are not fixed but run with the energy scale. At higher energies, such as those present in the early Universe, these couplings (or, the strength of the forces) become more similar, allowing the different forces to behave as a single unified interaction at a grand unification scale of order 10^{15} GeV ($\sim 10^{-4}$ of the Planck mass) [4].

The subsequent evolution of the Universe therefore involved a hierarchy of symmetry-

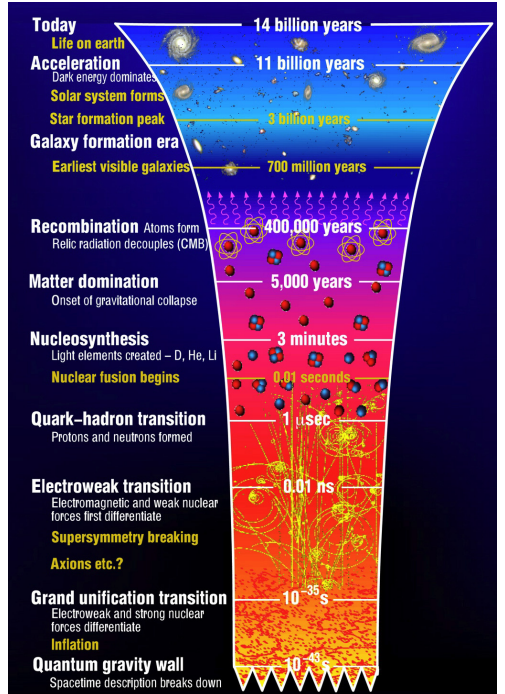


Figure 1: Brief history of the universe: different symmetry-breaking epochs at early universe. (Source)

breaking events. A convenient and physically transparent way to describe symmetry breaking during these cosmological phase transitions is through a Higgs-type scalar field ϕ . For illustrative purposes, consider a simple theory with symmetry group $G = U(1)$ and a complex scalar field governed by the self-interaction potential [5],

$$V(\phi) = \frac{\lambda}{4} (\phi^\dagger \phi - \eta^2)^2. \quad (1)$$

At zero temperature, the minima of this potential occur at nonzero field values $|\phi| = \eta$, indicating spontaneous symmetry breaking. The field acquires a vacuum expectation value $\langle\phi\rangle = \eta e^{i\theta}$, where the magnitude is fixed but the phase θ is arbitrary. Consequently, the set of degenerate vacuum states forms a continuous vacuum manifold, which in this case corresponds to a circle in the complex ϕ plane.

In the hot early Universe, however, thermal effects play a crucial role. At finite temperature, the effective potential for ϕ receives additional contributions from interactions with the thermal bath. In the high-temperature limit, this effective potential can be written as,

$$V_T(\phi) = AT^2\phi^\dagger\phi + V(\phi), \quad (2)$$

which introduces a temperature-dependent mass term (quadratic term of equation-2) $m^2(T) = AT^2 - \lambda\eta^2$. Here the dimensionless constant A is a combination of the self-coupling λ and other couplings of the field ϕ (e.g., Yukawa couplings and gauge coupling). For temperatures above the critical value $T_c = \eta\sqrt{\lambda/A}$, the mass squared is positive and the effective potential is minimized at $|\langle\phi(T > T_c)\rangle| = 0$, corresponding to a symmetric phase. As the Universe cools and the temperature drops below T_c , the mass squared becomes negative, rendering the symmetric state unstable and driving the field toward a new minimum with a non-zero expectation value given by,

$$|\langle\phi(T < T_c)\rangle|^2 = \left(\eta^2 - \frac{A}{\lambda}T^2\right) = \eta^2 \left(1 - \frac{T^2}{T_c^2}\right) \quad \{A > 0\} \quad (3)$$

This marks the onset of spontaneous symmetry breaking and a qualitative change in the vacuum structure.

The first major transition involved the breakdown of the GUT symmetry to the Standard Model symmetries, likely depositing massive topological defects. This was followed much later by electroweak symmetry breaking at an energy scale of approximately 100 GeV [4]. These transitions represent dramatic changes in the vacuum structure of the Universe and underpin several fundamental phenomena, including the generation of particle masses through the Higgs mechanism (see figure-2) and the emergence of the observed baryon asymmetry through mechanisms involving CP violation. A fundamental constraint governing these transitions is causality; physical effects cannot propagate faster than the speed of light, c . Consequently, at any given time t , regions of the Universe separated by a distance greater than the horizon distance $d = ct$ are causally disconnected.

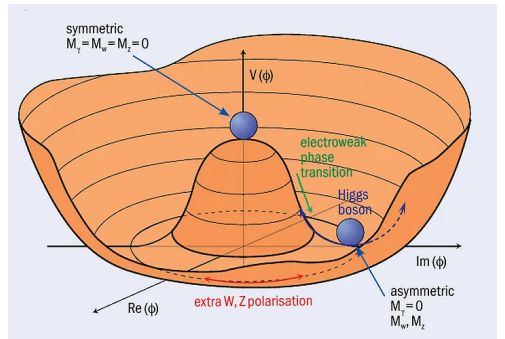
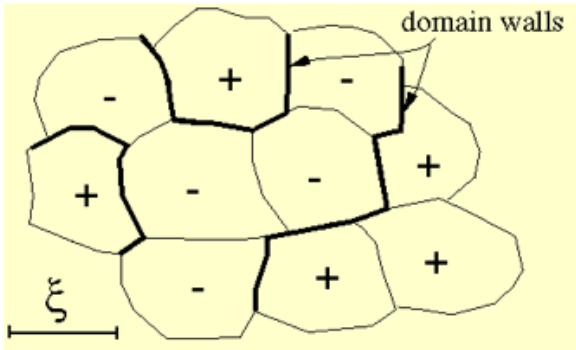


Figure 2: Spontaneous symmetry breaking of the Higgs field below the critical temperature, resulting in the generation of massive excitations via the Higgs mechanism. ([Source](#))

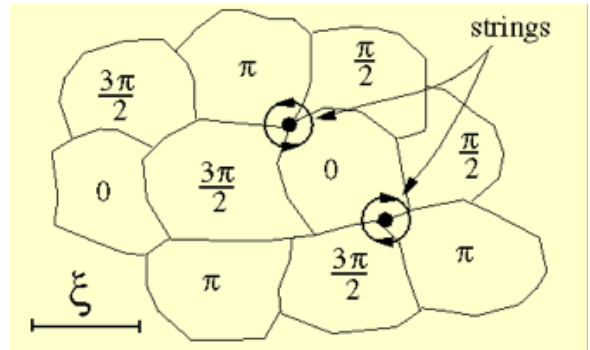
During a symmetry-breaking phase transition, these isolated regions must independently decay into a specific minimum energy state within the vacuum, \mathcal{M} . Due to the stochastic nature of this process, causally separated regions often settle into different vacuum states, much like crystallizing ice forming misaligned grains. The boundaries between these misaligned regions manifest as topological defects [6]. These are stable configurations of energy, formed where the vacuum choices of neighboring regions cannot be smoothly reconciled.

To understand the variety of defects that can emerge, one must look at the specific geometry of the potential landscape. In a simplified model with two distinct minima (e.g., positive and negative states), a domain wall forms at the interface. In theories where the vacuum manifold has a complex topology, specifically containing holes or non-contractible loops, the underlying field can wrap around these topological features. This wrapping creates a mismatch in the field's orientation, resulting in stable, linear defects of trapped high energy known as cosmic strings [5]. The specific nature of these defects, whether they manifest as surfaces (domain walls), lines (cosmic strings), or points (monopoles), depends strictly on the topology of the broken symmetry group.

Mathematically, this dependency is classified using homotopy groups, $\pi_n(\mathcal{M})$, which describe the connectivity of the vacuum manifold defined as the quotient space, $\mathcal{M} = G/H$. Here, G represents the full, underlying symmetry group of the high-energy theory and H denotes the subgroup of symmetries that remain unbroken in the vacuum state. For instance, a disconnected manifold ($\pi_0(\mathcal{M}) \neq \mathbb{I}$) yields domain walls, a manifold with non-contractible loops ($\pi_1(\mathcal{M}) \neq \mathbb{I}$) produces cosmic strings, and non-contractible 2-spheres ($\pi_2(\mathcal{M}) \neq \mathbb{I}$) result monopoles. Furthermore, if the manifold supports non-trivial mappings of the 3-sphere ($\pi_3(\mathcal{M}) \neq \mathbb{I}$), the resulting defects are known as textures, which manifest as unstable, twisted field configurations rather than singular boundaries.



(a) The Kibble mechanism for the formation of domain walls. (Source- [6])



(b) The Kibble mechanism for the formation of cosmic strings. (Source- [6])

The cosmological implications of topological defects are strictly dependent on the specific symmetry broken. Defects such as domain walls and magnetic monopoles possess such massive energy densities that their existence would dominate the universal energy budget, leading to evolution scenarios that contradict observational data [6]; models predicting these are therefore largely ruled out. Conversely, cosmic strings are cosmologically viable. They may have served as gravitational “seeds” for large-scale structure formation [5, 7], contributed to anisotropies in the Cosmic Microwave Background (CMB), and could potentially account for a portion of the universe’s dark matter.

Consequently, topological defects provide a unique observational window [8] into the physics of the extremely early Universe, an energy scale inaccessible to terrestrial particle accelerators. However, to rigorously evaluate these scenarios, a precise understanding of de-

fect dynamics is required. Before current observations can be used to constrain high-energy theory, it is imperative to develop a robust model of how cosmological defects evolve and interact throughout cosmic history.

1.2 Kibble-Zurek mechanism

The Kibble-Zurek mechanism (KZM) is a theoretical framework that unifies the non-equilibrium dynamics of symmetry-breaking phase transitions across vastly different energy scales. Originally proposed by T.W.B. Kibble to explain the formation of cosmological defects in the early universe [1], the theory was later extended by W.H. Zurek to condensed matter systems [9, 10]. By relying on the universality of critical dynamics, the KZM links cosmological topological defects to accessible laboratory analogues like vortices in superfluids or disclinations in liquid crystals [11–16].

The Nematic Order Parameter: To apply this universal framework to the specific case of liquid crystals, we must first define the physical system. Liquid crystals [11, 17, 18] constitute a class of organic systems that exhibit distinct mesophases intermediate between isotropic liquids and crystalline solids, characterized by long-range orientational order described by a director field $\mathbf{n}(\mathbf{r})$.

The key feature of this order parameter is its symmetry. In the high-temperature isotropic phase, the molecules are randomly oriented, possessing full rotational symmetry ($O(3)$). As the system cools into the nematic phase, this symmetry breaks, and the molecules align along a common axis. However, because the molecules are non-polar (head-to-tail symmetric), the states \mathbf{n} and $-\mathbf{n}$ are physically indistinguishable. This specific symmetry breaking ($O(3) \rightarrow O(2)$) creates a complex “vacuum manifold” that allows for the formation of stable topological defects, specifically the $\pm 1/2$ disclination strings.

Any distortion in this alignment costs energy, quantified by the Frank elastic free energy, F . In its general form, the free energy density is given by ,

$$F = \frac{1}{2} \left\{ K_1 (\nabla \cdot \mathbf{n})^2 + K_2 (\mathbf{n} \cdot \nabla \times \mathbf{n})^2 + K_3 |\mathbf{n} \times \nabla \times \mathbf{n}|^2 \right\} \quad (4)$$

where K_1 , K_2 , and K_3 are the splay, twist, and bend elastic constants.

Because liquid crystals are highly viscous, inertial effects are negligible. The director field therefore evolves purely to minimize the free energy, balancing viscous drag against elastic forces. The general equation of motion is [13],

$$\gamma \frac{\partial n_\alpha}{\partial t} = - \frac{\delta F}{\delta n_\alpha} \quad (5)$$

where γ is the rotational viscosity and the derivative includes the constraint $|\mathbf{n}|^2 = 1$.

By applying the “one-constant approximation” ($K_1 = K_2 = K_3 = K$), this simplifies to the *damped nonlinear sigma model* which is similar to the nonlinear sigma model used by cosmologists to study the evolution of a universe populated by global defects [13]:

$$\gamma \frac{\partial n_\alpha}{\partial t} = K \left[\nabla^2 n_\alpha + (\nabla n_\beta) \cdot (\nabla n_\beta) n_\alpha \right] \quad (6)$$

This diffusive equation governs the relaxation process that drives the late-time coarsening of the defect network.

1.2.1 Defect formation dynamics

With the system defined, we can now predict how defects form during the transition. The core quantitative prediction of the KZM describes how the density of resulting defects scales with the speed of the transition. Consider a continuous phase transition driven by a control parameter $\epsilon(t)$, such as reduced temperature $|T - T_c|/T_c$, pressure, or electric field, that varies linearly with time t across the critical point at $t = 0$:

$$\epsilon(t) = \frac{|t|}{\tau_Q} \quad (7)$$

Here, τ_Q represents the characteristic quench timescale; a smaller τ_Q implies a faster transition.

As the system approaches the critical point, its internal dynamics slow down significantly. According to Landau-Ginzburg theory, the equilibrium relaxation time $\tau(t)$ and the correlation length $\xi(t)$ diverge as functions of the control parameter,

$$\tau(t) \propto |\epsilon(t)|^{-\nu z} \quad (8)$$

$$\xi(t) \propto |\epsilon(t)|^{-\nu} \quad (9)$$

where ν is the correlation-length critical exponent and z is the dynamical critical exponent.

The system can maintain equilibrium only as long as its relaxation time $\tau(t)$ is faster than the time scale on which the environment is changing, represented by the time remaining until the transition $|t|$. As $\tau(t)$ diverges near the critical point, it inevitably overtakes $|t|$. At this moment, the system's reaction time becomes too slow to adapt to the changing conditions, and the domain structure effectively “freezes”. This “freeze-out” occurs at a characteristic time \hat{t} when the two timescales become comparable,

$$\tau(\hat{t}) \approx \hat{t} \quad (10)$$

By substituting the power-law dependence of the relaxation time into this condition, we can solve for the freeze-out time \hat{t} in terms of the quench rate,

$$\tau(\hat{t}) = \left(\frac{\hat{t}}{\tau_Q} \right)^{-\nu z} \propto \hat{t} \implies \hat{t} \propto \tau_Q^{\frac{\nu z}{1+\nu z}} \quad (11)$$

Consequently, the control parameter at freeze-out scales as,

$$\hat{\epsilon} = \epsilon(\hat{t}) \propto \tau_Q^{-\left(\frac{1}{1+\nu z}\right)} \quad (12)$$

The density of the resulting topological defects is determined by the configuration of the system at the moment of freeze-out. The characteristic size of the ordered domains is set by the correlation length $\hat{\xi}$ at time \hat{t} ,

$$\hat{\xi} = \xi(\hat{t}) \propto |\hat{\epsilon}|^{-\nu} \propto \left(\tau_Q^{-\left(\frac{1}{1+\nu z}\right)} \right)^{-\nu} \propto \tau_Q^{\frac{\nu}{1+\nu z}} \quad (13)$$

Assuming that defects form at the boundaries of these domains, the initial defect density ρ scales inversely with the volume (or area) of the domains. If d is the effective dimension of

the defect (where $d = D_{\text{space}} - D_{\text{defect}}$), then $\rho \propto \hat{\xi}^{-d}$. This yields the Kibble-Zurek scaling law for defect formation,

$$\rho \propto \tau_Q^{-\frac{d\nu}{1+\nu z}} \quad (14)$$

This equation predicts a universal power-law dependence on the quench rate. For example, in a mean-field transition (where $\nu = 1/2$ and $z = 2$) producing line defects in three dimensions ($d = 2$), the exponent simplifies to the standard result often cited in literature [8, 19],

$$\rho \propto \tau_Q^{-1/2} \quad (15)$$

This scaling law has been experimentally verified in diverse systems, providing strong evidence for the universality of the mechanism.

1.2.2 Late-time coarsening dynamics

Following their formation, the defect network evolves to minimize the system's Frank elastic free energy. This process is effectively described by the "one-scale" model, which simplifies the complex network by assuming it is defined by just one characteristic length, $\xi(t)$, that changes with time. This scale $\xi(t)$ simultaneously represents the typical radius of curvature of the defects and the average separation distance between them.

In condensed matter systems, such as nematic liquid crystals, the motion of defects is typically overdamped, meaning that frictional forces dominate over inertial effects. Strictly speaking, the string line tension is proportional to $\ln(R/R_c)$, where R is the radius of the disclination line (essentially the distance to the nearest neighbor, $R \approx \xi$) and R_c is the core radius [13]. Similarly, the viscous dissipation is proportional to $\ln(R/R_c)$. However, because these logarithmic dependences are weak functions of R , to a good approximation one can model the dynamics of a string as having a constant line tension T and a constant mobility related to the friction coefficient per unit length Γ .

Under this approximation, the dynamics are governed by the balance between two competing forces per unit length. The tension force F_T , which acts to straighten curved defect segments, scales inversely with the local curvature radius ξ ,

$$F_T \approx \frac{T}{\xi} \quad (16)$$

Opposing this motion is the frictional drag force F_f , arising from the fluid viscosity, which is proportional to the defect velocity v ,

$$F_f \approx \Gamma v \quad (17)$$

By equating these forces ($F_T \approx F_f$), we determine the characteristic terminal velocity [11] of the defect network,

$$v \approx \frac{T}{\Gamma \xi} \quad (18)$$

As the network coarsens, energy is dissipated through friction. The rate of energy loss per unit volume, dW/dt , corresponds to the work done against the frictional force. For a defect network with density $\rho \approx \xi^{-d}$ (where d is an effective dimension scaling exponent), the power dissipated is,

$$\frac{dW}{dt} \approx -(F_f v) \rho \approx -(\Gamma v^2) \frac{1}{\xi^d} \quad (19)$$

Substituting the expression for the characteristic velocity we have,

$$\frac{dW}{dt} \approx -\Gamma \left(\frac{T}{\Gamma \xi} \right)^2 \frac{1}{\xi^d} = -\frac{T^2}{\Gamma \xi^{d+2}} \quad (20)$$

The total energy density of the network is given by $W \approx T\rho$. Consequently, the rate of energy loss is directly proportional to the rate of change in defect density,

$$\frac{dW}{dt} = T \frac{d\rho}{dt} \quad (21)$$

By equating the two expressions for energy dissipation and expressing the length scale in terms of density (noting that $\xi^{-(d+2)} = (\rho^{1/d})^{d+2} = \rho^{\frac{d+2}{d}}$), we obtain the evolution equation,

$$T \frac{d\rho}{dt} \approx -\frac{T^2}{\Gamma} \rho^{\frac{d+2}{d}} \Rightarrow \frac{d\rho}{dt} \propto -\rho^{\frac{d+2}{d}} \quad (22)$$

For the specific case of line defects (strings) in three dimensions, the defect density is defined as length per unit volume, which corresponds to $d = 2$ (since $\rho \propto \xi^{-2}$). Substituting $d = 2$ into the evolution equation yields $d\rho/dt \propto -\rho^2$. Integrating this differential equation leads to the universal scaling law for late-time dynamics,

$$\boxed{\rho(t) \propto t^{-1}} \quad (23)$$

For domain walls ($d = 1$) in two or, three dimensions this becomes,

$$\boxed{\rho(t) \propto t^{-\frac{1}{2}}} \quad (24)$$

1.3 Project objectives

This work establishes nematic liquid crystals [17] as a robust laboratory platform for investigating the dynamics of topological line defects (strings), providing a direct analogue to those predicted in early-universe cosmology. The primary objective is to experimentally validate the Kibble-Zurek mechanism (KZM), which governs defect production during symmetry-breaking phase transitions, and the one-scale scaling model.

We specifically test quantitative KZM predictions by performing electric-field quenches at varying rates τ_Q , aiming to confirm the defect density scaling $\rho(0) \propto \tau_Q^{-1/2}$. High-speed videography is employed to capture the full temporal evolution of the defect network, from initial formation through late-time coarsening. The experimental methodology is detailed in Section 2, followed by the computational image analysis framework in Section 3. Finally, we present our quantitative outcomes in Section 4 and conclude with a discussion of implications in Section 5.

2 Experimental Setup

We employ liquid crystals for this study because they occupy a unique experimental advantage. Unlike ordinary fluids (e.g., water), which lack internal directional structure and thus cannot support topological defects in the fluid phase, liquid crystals possess the continuous symmetry breaking essential for simulating cosmic string formation. Furthermore, unlike quantum fluids (e.g., superfluid helium), which require extreme cryogenic environments, liquid crystals exhibit defect dynamics on accessible macroscopic timescales under ambient conditions.

The experiment utilizes a homeotropic alignment, where molecules are anchored perpendicular to the substrate. In this uniform state, the system appears optically isotropic. However, during rapid phase transitions (quenches), topological defects form where the local order is disrupted. Due to the material's birefringence, the rapidly twisting director field near these defects creates sharp refractive index gradients. These gradients act as cylindrical lenses, refracting incident light away from the microscope's collection aperture, manifesting as distinct dark strings against a bright background. This high-contrast visualization enables precise tracking of the defect network. Because the topological constraints of liquid crystals map directly onto high-energy field theories, this system serves as a rigorous laboratory analogue for verifying the Kibble-Zurek mechanism and the non-equilibrium dynamics of cosmic strings.

2.1 Preparing empty cell

Preparation of liquid crystal cells follows a series of well-established, standardized steps. The standard workflow is outlined below.

2.1.1 Patterning:

ITO-coated glass slides are cut and patterned to create defined electrode regions. The glass is placed on a cutting mat and the non-coated side is cut to $4\text{ cm} \times 2\text{ cm}$ dimensions. A multimeter verifies the coated side. The coated surface is then marked with 1 cm wide cello tape, leaving 0.5 cm gaps at both ends. This protects the desired conducting area.

2.1.2 Etching:

In a fume hood, concentrated HCl and zinc powder are added to a beaker containing the patterned glass (coated side up). The mixture etches the exposed ITO for 30 minutes, removing it from unprotected areas while leaving the tape-covered region intact. After etching, the glass is carefully removed with tweezers and rinsed thoroughly with distilled water and a dilute base to neutralize all acid residue. The glass is dried and transferred to the cleaning stage.

2.1.3 Post etching treatment:

The etched glass is cut vertically down the middle to produce two symmetric slabs. Both slabs are scrubbed with soap and isopropyl alcohol (IPA) to remove loose particles. They are then placed in a petri dish with a soap-water mixture and sonicated for 15 minutes at $40\text{--}50^\circ\text{C}$. After sonication, the slabs are rinsed with fresh IPA and dried with nitrogen gas, ensuring no residue remains.

2.1.4 Applying surfactant (DMOAP):

A 0.2% DMOAP surfactant solution is prepared by mixing 160 μL of DMOAP with 80 mL of distilled water. The glass slabs are held vertically and dipped into this solution for 5 minutes, allowing the methoxy groups of the surfactant to hydrolyze and form hydrogen bonds with the hydroxyl groups naturally present on the glass surface. The slabs are then rinsed with distilled water, dried with nitrogen gas, returned to the petri dish, and baked in a hot air oven at 110°C for 60 minutes. This thermal treatment drives a condensation reaction that converts the initial hydrogen bonds into robust, covalent siloxane (Si-O-Si) linkages. These bonds rigidly anchor the long alkyl chains perpendicular to the substrate, creating a steric barrier that induces the desired homeotropic alignment of the liquid crystal molecules.

2.1.5 Cell assembly:

Both treated slabs are assembled as a sandwich with spacer beads (23 μm diameter) placed 1 cm apart around the edges. The spacers create a uniform gap between the glass plates. The assembled cell is pressed moderately for 30 minutes to stabilize the spacers. The cell edges are then sealed with epoxy and allowed to cure thoroughly for at least a day to ensure a strong bond. Once the epoxy is fully set, electrical wires are connected to the ITO electrodes by carefully soldering with indium.

2.2 Capacitance-based cell thickness measurement

The thickness of the liquid crystal cell was determined using a capacitance-based measurement technique. The cell was modeled as a parallel-plate capacitor, for which the capacitance C is related to the cell thickness d by

$$d = \frac{\varepsilon_0 \varepsilon_r A}{C}, \quad (25)$$

where ε_0 is the vacuum permittivity, ε_r is the relative permittivity (taken to be ≈ 1 for air), and A denotes the effective electrode area.

Capacitance measurements were performed using a precision LCR meter. To accurately estimate the effective area, only the region of overlap between the patterned ITO electrodes was considered, while edge regions and spacer areas were excluded to minimize systematic errors.

For an effective electrode area of $(8.0 \pm 0.4) \times 10^{-5} \text{ m}^2$, the measured capacitance was $C = 16.23 \text{ pF}$. Substituting these values into above equation yields a cell thickness of

$$d = 43.62 \pm 2.18 \mu\text{m}. \quad (26)$$

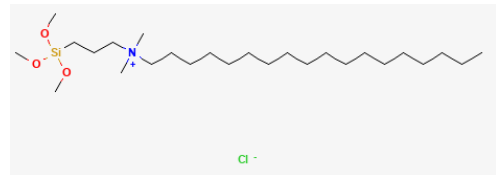


Figure 3: DMOAP structure ($C_{26}H_{58}CLNO_3Si$) ([Source](#))

2.3 Preparing homeotropic cell

The assembled LC cell is placed on a temperature control device programmed with a three-stage thermal protocol:

1. heat to $50^{\circ}C$ at a rate $20^{\circ}C/min$ and hold for 10 mins,
2. cool to $36^{\circ}C$ at a rate $1^{\circ}C/min$ and hold for 5 mins,
3. cool to $25^{\circ}C$ at a rate $0.1^{\circ}C/min$ and hold.

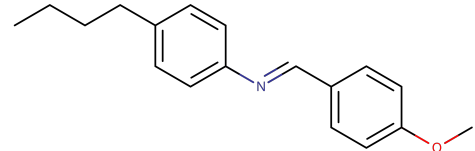


Figure 4: MBBA ([Source](#))

Once the device reaches $50^{\circ}C$, a small drop of MBBA liquid crystal is carefully placed on the cell edge using a lab spatula. As the MBBA warms and becomes transparent, it is gently pushed toward the cell center, where capillary action draws it throughout the cell gap. The lid is closed, and the cell is left undisturbed for at least 24 hours during the slow cooling protocol, allowing the liquid crystal to reach the nematic phase and establish uniform homeotropic alignment with minimal defects. Upon completion, the cell is inspected under crossed polarizers to verify uniform alignment and is then ready for experimental use or stored in a sealed container at room temperature.

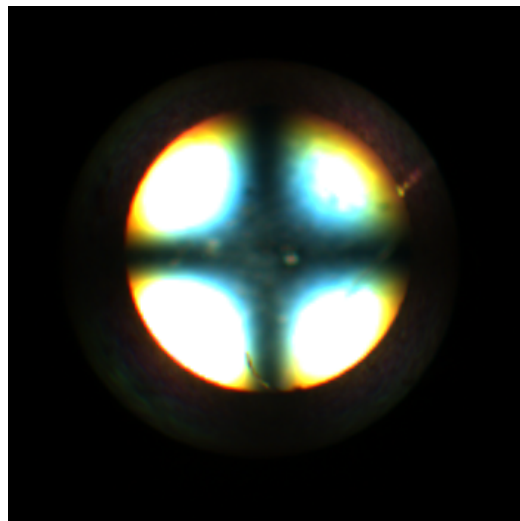


Figure 5: Conoscopic image confirming the homeotropic alignment of the liquid crystal cell.

2.4 Optical microscopy system

Electrodes from the function generator, which delivers an RMS AC sine wave voltage ranging from 10V to 60V at 10kHz via an A800DI high voltage linear amplifier, were connected to the cell. At a controlled temperature of $28^{\circ}C$, dynamic data of defect dynamics were recorded under $10\times$ magnification for RMS voltages of 10V, 20V, 40V, and 60V. For defect formation studies, an electric-field ramp was implemented using a 10 kHz sawtooth waveform, with the peak-to-peak voltage V_{pp} systematically varied across 200, 300, 400, 500, 600, 700, 800, and 900 mV to enable controlled traversal of the instability threshold.

3 Computational Framework

Captured frame images are subsequently processed through a series of image analysis operations using the Python Sci-kit Image [20] package. The detailed analysis framework¹ is described below.

3.1 Pre-processing and noise reduction

In the first step of image processing, we have implemented a 3×3 median filter to reduce noise and improve the overall quality of the image. The median filter is a non-linear filtering technique that replaces each pixel value with the median of the intensity values within its 3×3 neighborhood. Specifically, for every pixel, a 3×3 window is centered on it, and the nine pixel values within this window are sorted in ascending order. The median value from this sorted list is then assigned to the central pixel, effectively suppressing impulsive noise such as salt-and-pepper noise while preserving important image details. Unlike linear filters that tend to blur edges by averaging pixel values, the median filter maintains sharp boundaries and fine structures, making it particularly effective for applications where edge preservation is crucial.

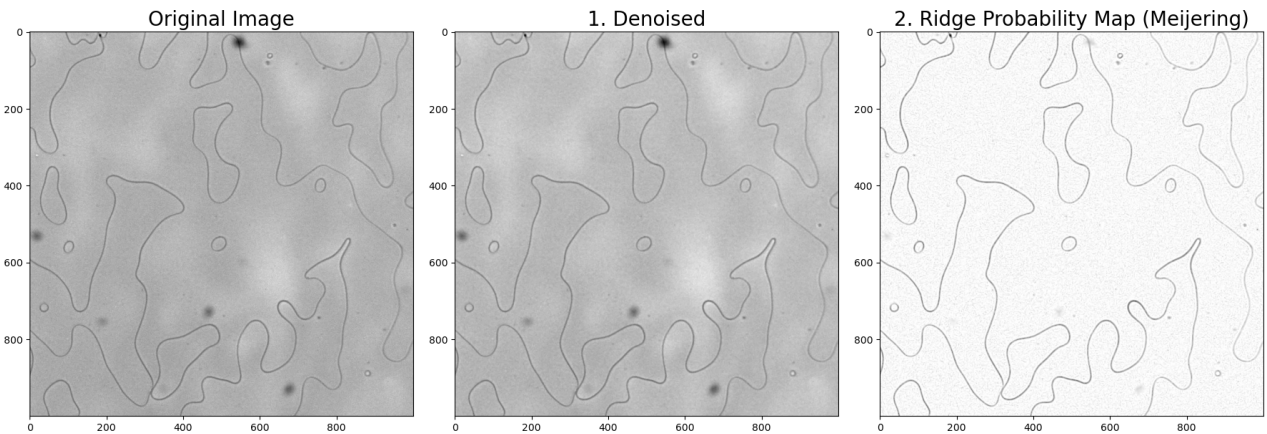


Figure 6: Images after 3×3 median noise filter and Meijering ridge detection. The sample image is a single frame from 60V at $10\times$ magnification.

3.2 Ridge detection operation

For ridge detection, we implement the Meijering ridge detection filter [21], a modified Hessian-based approach specifically designed to detect elongated, tubular structures in noisy images. In this implementation, the required second-order image derivatives $f_{ij}(\mathbf{x})$ are computed by convolving the image f with the second-order derivatives of a normalized Gaussian kernel G , expressed as $f_{ij}(\mathbf{x}) = (f * G_{ij})(\mathbf{x})$, where $G_{ij}(\mathbf{x}) = \left(\frac{\partial^2 G}{\partial_i \partial_j} \right)(\mathbf{x})$ and $\mathbf{x} = (x, y)$ denotes the pixel position. The eigenvectors and eigenvalues are determined not from a standard Hessian, but from a modified matrix $\mathbf{H}'_f(\mathbf{x})$:

¹Framework scripts, notebooks and analysis results can be found here: [Repository](#)
Clone: `$ git clone https://github.com/mandal-anik10/SLP-CosmoWithLCs.git`

$$\mathbf{H}'_f(\mathbf{x}) = \begin{bmatrix} f_{xx}(\mathbf{x}) + \alpha f_{yy}(\mathbf{x}) & (1 - \alpha) f_{xy}(\mathbf{x}) \\ (1 - \alpha) f_{xy}(\mathbf{x}) & f_{yy}(\mathbf{x}) + \alpha f_{xx}(\mathbf{x}) \end{bmatrix}$$

where α is a weighting parameter (typically set to 1/3 for 2D images ([Source](#))) that ensures the filter is maximally flat in the longitudinal direction of the ridge. The normalized eigenvectors $\mathbf{v}'_i(\mathbf{x})$ of this modified matrix remain identical to the standard Hessian eigenvectors $\mathbf{v}_i(\mathbf{x})$, while the modified eigenvalues $\lambda'_i(\mathbf{x})$ are calculated as $\lambda'_1(\mathbf{x}) = \lambda_1(\mathbf{x}) + \alpha\lambda_2(\mathbf{x})$ and $\lambda'_2(\mathbf{x}) = \lambda_2(\mathbf{x}) + \alpha\lambda_1(\mathbf{x})$. The filter assigns a “neuriteness” or “vesselness” measure $\Phi(x)$ to each pixel according to $\Phi(x) = \lambda(x)/\lambda_{\min}$ for $\lambda(x) \geq 0$ and $\Phi(x) = 0$ otherwise, where λ represents the larger modified eigenvalue in magnitude and λ_{\min} is the minimum eigenvalue across all pixels. By utilizing the eigenvector corresponding to the smaller absolute eigenvalue to indicate the longitudinal direction, this method effectively suppresses responses to background intensity discontinuities while enhancing continuous, filamentous features. This multi-scale approach proves superior to basic Hessian or Laplacian-based detectors for identifying nematic liquid crystal defects, as it maintains connectivity across regions of varying contrast and width while significantly reducing false detections from noise artifacts.

3.3 Calculating defect density

A sequence of processing operations was applied to the ridge maps to robustly isolate defect lines from the background and to accurately quantify their total length and resulting line density.

3.3.1 Hysteresis thresholding:

To distinguish true ridge structures from spurious noise artifacts in the ridge-detected images, we apply hysteresis thresholding with two carefully selected thresholds, $T_{\text{high}}^{\text{2}}$ and $T_{\text{low}}^{\text{2}}$, following the methodology established in the Canny edge detection framework [[22](#)]. In this dual-threshold approach, pixels with ridge metric values above T_{high} are immediately classified as definite defect pixels (strong edges), while those below T_{low} are rejected as background. Critically, pixels with values between T_{low} and T_{high} (weak edge pixels) are retained only if they remain connected to already-classified defect pixels through 8-connectivity neighborhoods.

3.3.2 Binary closing and removing small objects:

To further refine the segmentation, binary morphological closing² (a dilation followed by an erosion) is applied to bridge small gaps and holes within detected defect regions, followed by connected component analysis to remove small objects below a chosen length threshold (**64px**); together, these steps ensure that only large, continuous defect structures are retained while isolated noise pixels and spurious fragments are effectively suppressed, resulting in cleaner and more accurate representations of the underlying defect network.

3.3.3 Skeletonizing:

The refined binary image containing identified defect regions is processed through skeletonization, a morphological thinning operation that reduces each detected defect lines to its medial axis; a connected, one-pixel-wide representation of the original structure. The

²Chosen thereshold parameter values and footprint size are given in the configuration file in the [repository](#).

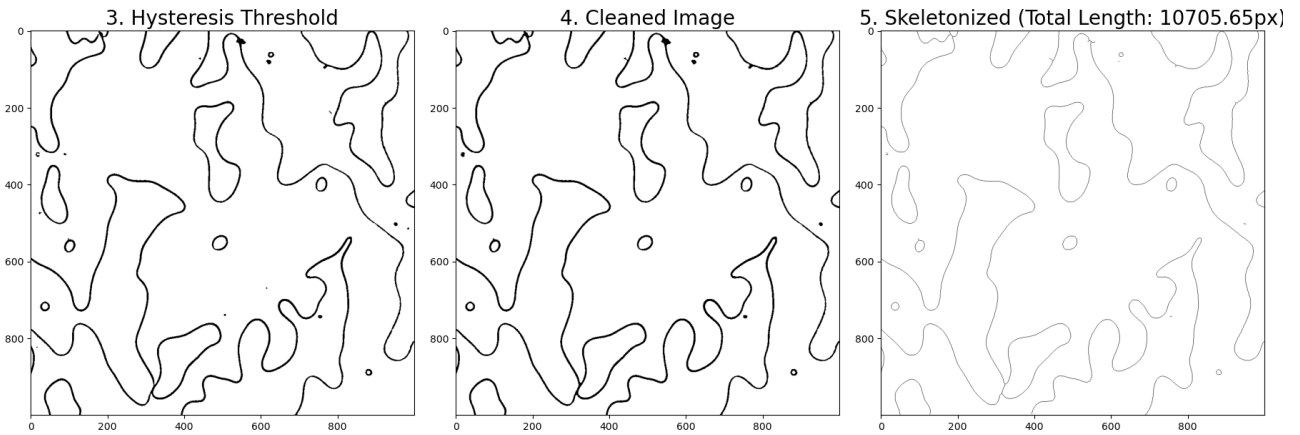


Figure 7: Images after hysteresis thresholding, binary closing, removing small objects, and skeletonizing. The sample image is a single frame from 60V at 10 \times magnification.

skeletonization algorithm iteratively removes boundary pixels from the binary image while preserving connectivity and topological properties, ensuring that the reduced skeleton maintains the same homotopy as the original object. This compact representation enables precise measurement of defect lengths and facilitates reliable analysis of defect network topology, even when original regions are wide or noisy.

To quantify the defect network from processed images, the total defect length is estimated by extracting the skeletonized form of each defect line and analyzing it with the *Skan* [23] library, which reconstructs the skeleton as a network graph and computes the sum of branch lengths using pixel connectivity and spacing. The cumulative length of all skeleton branches in the field of view directly yields the projected defect length L . To obtain the defect density ρ , this total length is divided by the sample volume V (the area imaged multiplied by the cell thickness), resulting in $\rho = L/V$.

4 Defect Dynamics

In the present study, the Fréedericksz transition was deliberately induced in a homeotropically aligned MBBA nematic liquid crystal cell in order to investigate defect formation and subsequent coarsening dynamics under an applied electric field. By using the electric field as a controlled external parameter, the transition provides a well-defined route to drive the system out of equilibrium and probe the emergence of topological defects.

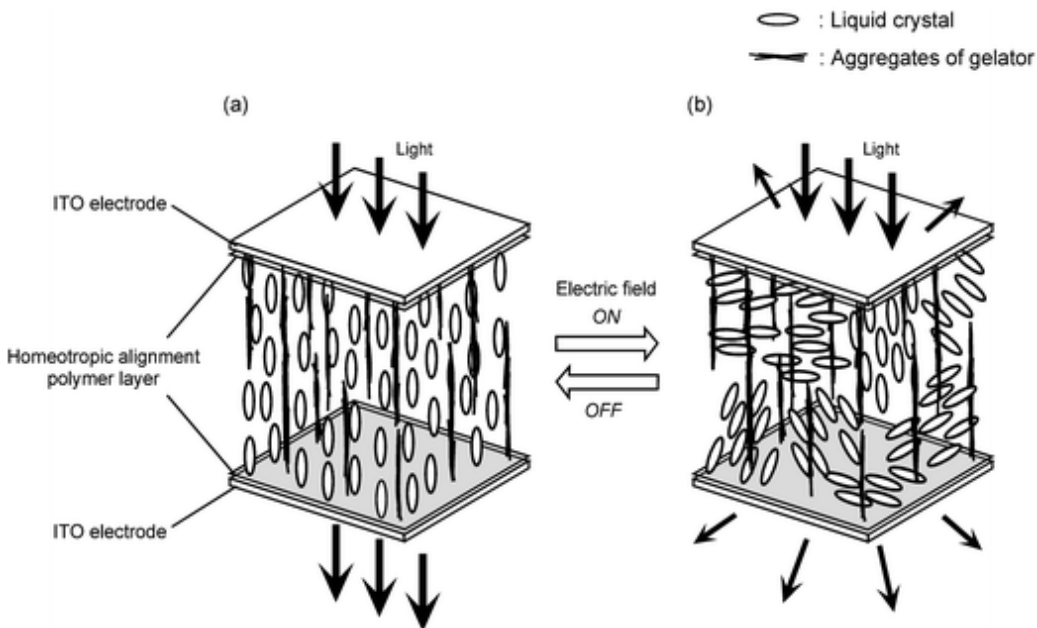


Figure 8: Fréedericksz transition in a homeotropically aligned nematic liquid crystal ([Source](#)).

4.1 The Fréedericksz transition

The Fréedericksz transition is a fundamental field-induced reorientation phenomenon in nematic liquid crystals, in which an initially uniform director configuration becomes unstable when an external electric or magnetic field exceeds a critical threshold. In a homeotropically aligned cell, the director is anchored perpendicular to the confining substrates in the absence of an applied field, resulting in a homogeneous alignment normal to the cell planes. When a destabilizing external electric field is applied, the torque exerted by the field on the anisotropic nematic medium competes with the elastic restoring forces associated with splay, twist, and bend deformations. Once the field strength exceeds the Fréedericksz threshold, the elastic energy can no longer sustain the uniform homeotropic state, and the director undergoes a continuous, spatially varying reorientation, developing in-plane components across the cell thickness (Figure 8).

The nature of this field-induced reorientation depends critically on the dielectric anisotropy of the nematic, defined as $\Delta\epsilon = \epsilon_{||} - \epsilon_{\perp}$. For materials with positive dielectric anisotropy ($\Delta\epsilon > 0$), the director tends to align parallel to the applied electric field to minimize dielectric energy. In contrast, for materials with negative dielectric anisotropy ($\Delta\epsilon < 0$), the director prefers to orient perpendicular to the applied field.

MBBA is a nematic liquid crystal with negative dielectric anisotropy; therefore, an applied electric field destabilizes the initial homeotropic alignment by favoring director orientations

perpendicular to the field. This setup serves as an ideal model for spontaneous symmetry breaking. Initially, the molecules stand vertically, possessing perfect rotational symmetry. When the applied voltage exceeds the critical threshold ($V > V_c$), this alignment becomes unstable. In a characteristic second-order transition, the magnitude of the director tilt increases continuously above this threshold. The instability is analogous to a ball balanced on the peak of a “Mexican Hat” potential, while the molecules are energetically compelled to tilt, every azimuthal direction is equally valid. Consequently, random thermal fluctuations cause separate regions to tilt in different directions, and the boundaries where these mismatched domains meet are where topological defects form.

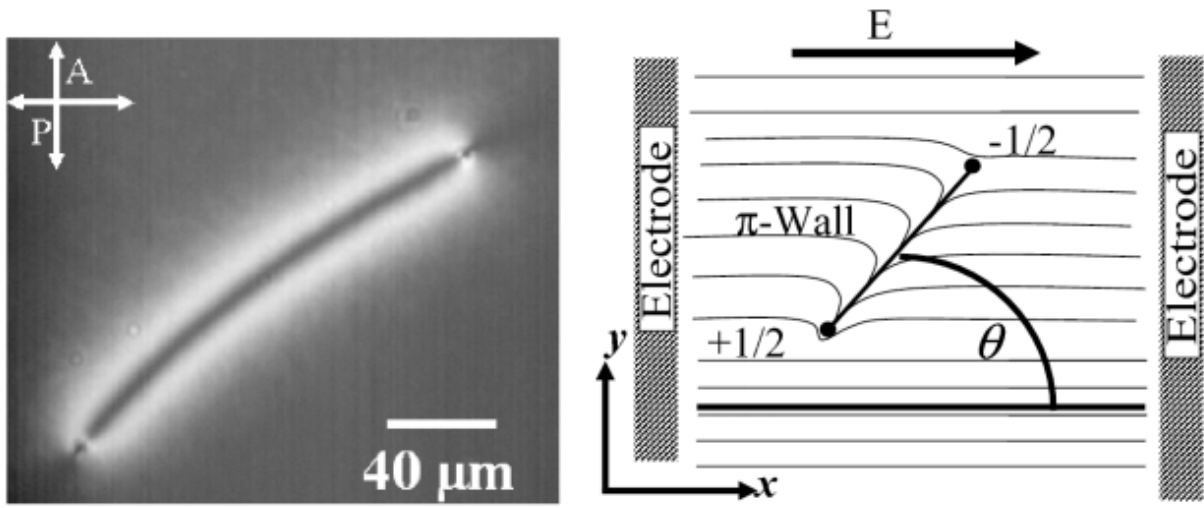


Figure 9: (Left) Observed under a cross polarizer, a pair of $\pm 1/2$ wedge disclinations connected by a π -wall when an in-plane electric field is present. (Right) Sketch of the 2D director field; θ is the angle between the π -wall and the electric field. (Source- [15])

For such an electric-field-driven transition in a homeotropic nematic cell, the critical voltage V_c is given, within the one-constant approximation, by

$$V_c = \pi \sqrt{\frac{K}{\varepsilon_0 |\Delta \varepsilon|}}, \quad (27)$$

where K is the Frank elastic constant, ε_0 is the vacuum permittivity, and $\Delta \varepsilon$ is the dielectric anisotropy of the liquid crystal.

This field-induced reorientation produces pronounced changes in optical birefringence and texture. The controllable instability associated with the Fréedericksz transition therefore provides an effective experimental parameter for probing defect formation and non-equilibrium dynamics in nematic liquid crystals.

4.2 Late-time coarsening dynamics

Observation and interpretation :

In the initial phase of this study, the prepared nematic liquid crystal cell (thickness $31.09 \pm 0.44 \mu\text{m}$) exhibited a significant population of permanent defects resulting from the sample preparation process. These pre-existing singularities served as effective nucleation sites

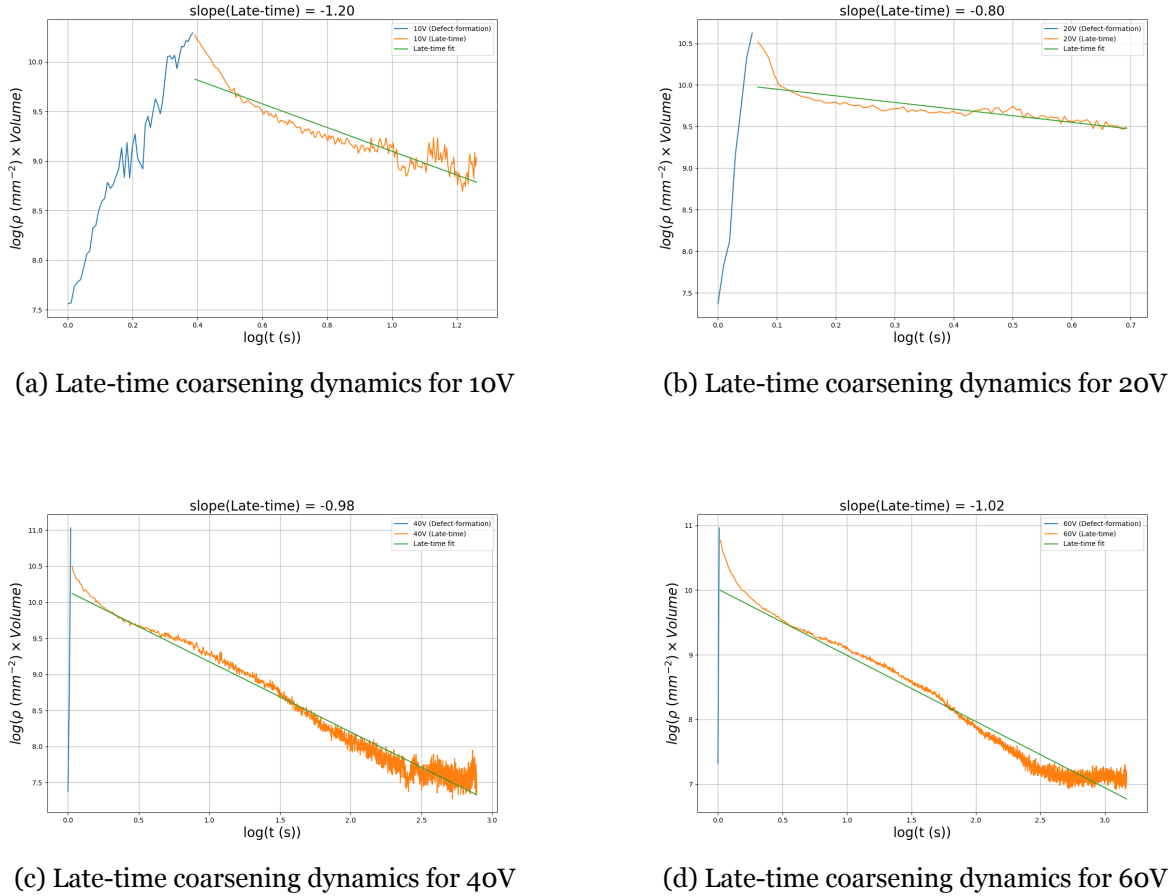


Figure 10: Old cell with permanent defects: Log-log plot showing the late-time coarsening dynamics of defect density (ρ) versus time (t) for the 10V, 20V, 40V, 60V applied field case, observed at $10\times$ magnification. The solid orange line represents the estimated defect length. The green line depicts the best power-law fit within the scaling regime.

for field-induced topological structures upon the application of the electric field. Consequently, the resulting defect network was characterized by the emergence of point defects with strength $\pm 1/2$, interconnected by π -walls (inversion walls), as illustrated in Figure 9 and Figure 16.

The subsequent evolution of this network was governed primarily by the elastic interactions and mutual annihilation of these line defects. Analysis of the late-time coarsening dynamics yielded scaling exponents of -1.20 at 10V, -0.80 at 20V, -0.98 at 40V, and -1.02 at 60V (see Figure 10). These values are in good agreement with the theoretical prediction of inverse-time scaling (t^{-1}) characteristic of string-dominated dynamics. The notable deviations observed at lower voltages (10V and 20V) can be attributed to reduced optical contrast and increased “fuzziness” of the defect lines, which compromised the robustness of the line-detection algorithm in this regime.

Regarding the uncertainty analysis for this dataset, it is important to note two limitations. First, random statistical errors could not be reliably estimated, as the data represents a single experimental realization for this sample. Second, uncertainties associated with the time variable were not accounted for in the extraction of the scaling exponents.

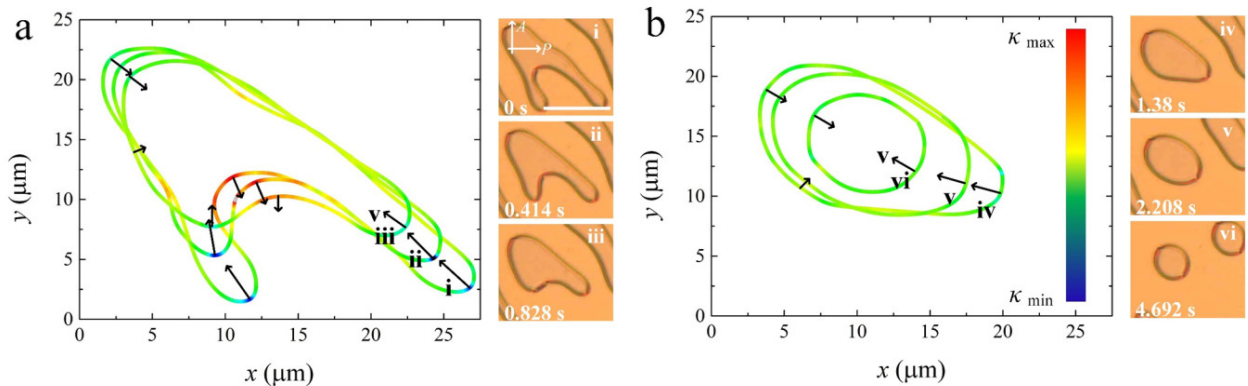


Figure 11: Shape evolution of a single domain at different moments and the corresponding polarizing optical microscope micrographs. (a) At the early stage of the annihilation, where the loop changes its shape drastically. (b) At the late stage of the annihilation, where the loop shrinks slowly with its shape unchanged. Black arrows indicate the velocities of different segments of the loop. The color of the loop indicates the local curvature. The color bar gives a linear scale of curvature κ . $\kappa_{min} = -1.24 \mu\text{m}^{-1}$ and $\kappa_{max} = 0.49 \mu\text{m}^{-1}$. (Source- [14])

To isolate the intrinsic defect formation and evolution dynamics, the experiment was repeated using a newly prepared liquid crystal cell with no observable permanent defects. In the absence of predefined nucleation sites, the system predominantly generated closed-loop, domain-wall-like defects in order to conserve topological charge. Such loop-dominated defect networks are expected to exhibit slower coarsening dynamics, with a theoretical scaling exponent close to -0.5 [14]. However, the measured exponents were substantially smaller (20V: -0.21 , 40V: -0.22 , 60V: -0.33), indicating that the early and intermediate-time dynamics are governed by fluctuation-dominated loop evolution rather than simple curvature-driven collapse.

At higher applied voltages, the strong dielectric torque confines the director more rigidly along the field direction, stabilizing the closed-loop topology and suppressing interactions with the cell boundaries. Consequently, these loop structures persist for extended durations (up to $\sim 15\text{--}20\text{s}$), as illustrated in figures-18, 19, and 20. At much later times ($\gtrsim 20\text{s}$), the loops occasionally open, most likely due to residual interactions with the substrates or weak quenched disorder in the bulk. This opening process converts closed loops into point defects connected by π -wall, triggering a crossover to faster, string-dominated coarsening dynamics. However, by this stage, the defect density is already very low, rendering statistical estimates of the scaling exponent unreliable.

In contrast, at 10V the weaker electric field provides less dielectric stabilization, allowing enhanced director fluctuations and earlier interactions with the cell boundaries. As a result, closed loops open at comparatively early times (figure-17), leading to a premature crossover to line-defect dynamics and a corresponding increase in the observed scaling exponent to -0.74 . Overall, these results show that the applied voltage controls how defect dynamics evolve, causing a transition from closed-loop defects to open line defects. This crossover is governed by the strength of the electric field, the presence of quenched disorder, and interactions with the cell boundaries, all of which determine the dominant coarsening mechanism and the observed scaling behavior.

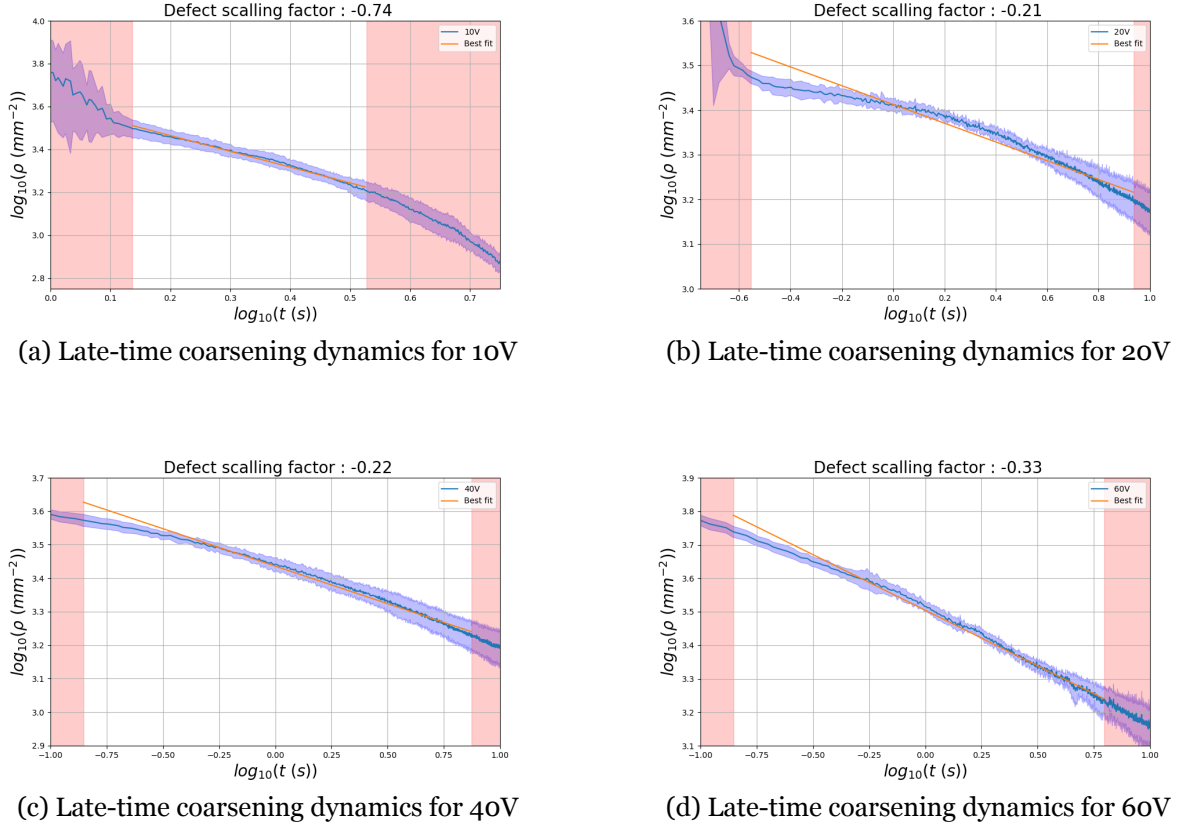


Figure 12: New cell without permanent defects: Log-log plot showing the late-time coarsening dynamics of defect density (ρ) versus time (t) for the 10V, 20V, 40V, 60V applied field case, observed at $10\times$ magnification. The solid blue line represents the average of the estimated defect length, with the surrounding shaded region indicating the 1σ limits of random error. The orange line depicts the best power-law fit within the scaling regime. The shaded red regions mark data excluded from the analysis: early-time data (left) were discarded to remove the initial 10–25 frames, while the late-time tail (right) was excluded based on relative error selection criteria.

4.3 Defect formation dynamics

Observation and interpretation :

For defect formation studies, an electric-field ramp was implemented using a 10 kHz sawtooth waveform, with the peak-to-peak voltage (V_{pp}) systematically varied across 200, 300, 400, 500, 600, 700, 800, and 900 mV to enable controlled traversal of the instability threshold. However, at this high frequency, the oscillation period of the electric field is significantly shorter than the characteristic relaxation time of the nematic director. Consequently, the system cannot react effectively to the instantaneous peak voltage, as the molecules are unable to reorient within the rapid oscillation cycles. This timescale mismatch causes the director field to fail to adiabatically follow the ramp, leading to an effective “freeze-out” of the dynamics. Instead of evolving through a critical phase transition, the system gets locked into a non-equilibrium state at a random finite length scale. As a result, the final defect structure is “immature,” governed principally by stochastic local factors rather than intrinsic physical laws. This mechanism explains the significant scatter in the defect density data observed in

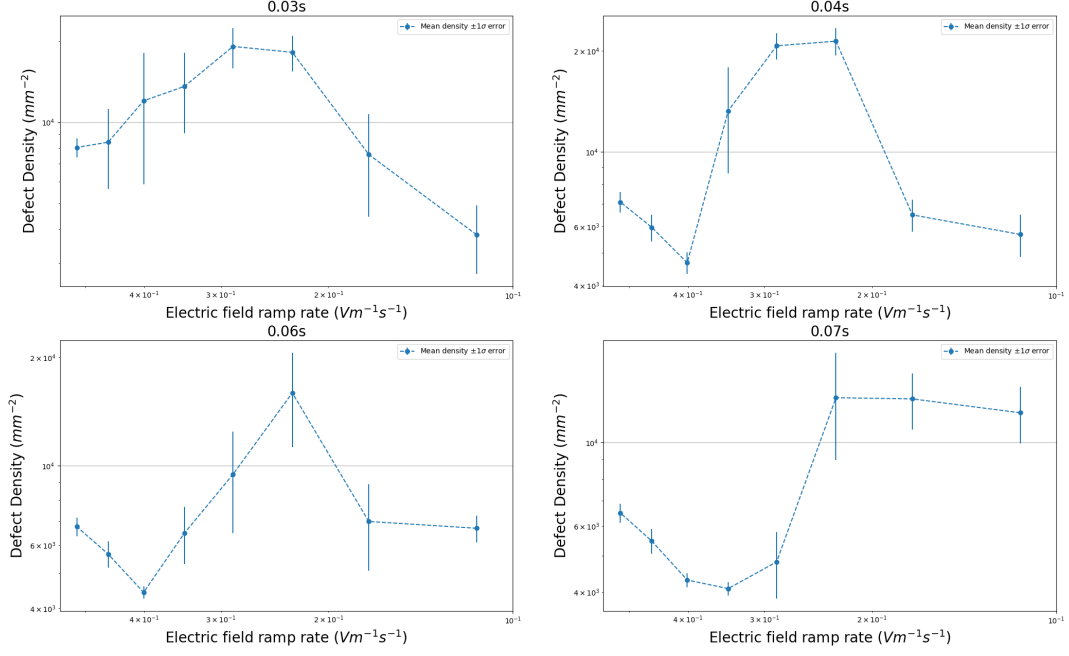


Figure 13: Analysis result from formation dynamics study. Defect densities have been plotted against the applied electric field ramp rate at 4 different initial time stamps.

figure- 13 and the absence of the power-law scaling expected from the Kibble-Zurek mechanism.

To overcome this freeze-out and allow the liquid crystal molecules sufficient time to respond to the applied field, the driving frequency was reduced. However, at lower frequencies (1–10 Hz), mobile ions within the liquid crystal are able to drift and accumulate, forming regions of excess charge. These charges interact with the electric field and drive fluid motion inside the cell. The resulting flow strongly distorts the molecular alignment, producing irregular and highly fluctuating optical textures that disrupt the ordered defect structures (as shown in the figure-14).

4.4 Error analysis

4.4.1 Error in time

Temporal uncertainty arises from a significant **30%** frame drop rate observed during the 100 fps recording process. This data loss is attributed to hardware bandwidth limitations, where the data write speed was insufficient to sustain the continuous storage of the high-frequency video stream. To reconstruct the true temporal evolution, a Monte Carlo resampling method was employed. The observed frame sequence was sequentially sampled 1000 times in the corrected time range (scaled by 100/70) to account for the stochastic nature of the drops. For each frame i , the median (μ_{t_i}) of the simulated arrival times was assigned as the corrected timestamp, while the standard deviation (σ_{t_i}) represents the temporal error:

$$t_i = \mu_{t_i} \pm \sigma_{t_i}$$

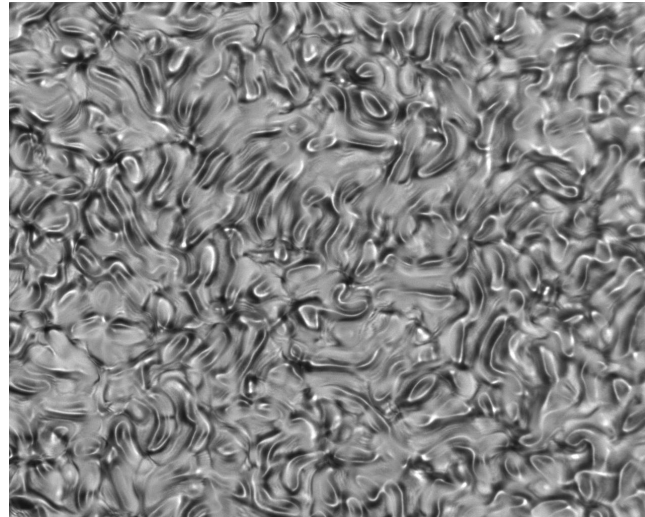


Figure 14: Electroconvection observed in the prepared MBBA Liquid crystal cell at applied electric field frequency of order $\sim Hz$ and applied voltage of order $\sim 10V$.

This statistical reconstruction mitigates the non-linear distortion introduced by the write-speed bottleneck.

Although the temporal uncertainty σ_{t_i} was rigorously calculated for every data point, horizontal error bars are omitted from the final plots to maintain graphical clarity. However, the analysis explicitly incorporates the corrected timestamps (μ_{t_i}) derived from the resampling procedure for the time axis. This ensures that the reported dynamics are grounded in the statistically reconstructed timeline, effectively acknowledging the latency-induced distortions.

4.4.2 Error in defect density

Systematic errors: The accuracy of the string defect density measurement is fundamentally limited by the precision of the geometric parameters used in the capacitance method. Specifically, a unit length measurement error of 2 mm introduces an uncertainty of 4 mm² in the unit area determination. Given the total measured sample area(A) of 80 mm², this corresponds to a relative fractional error of 5%. This geometric uncertainty propagates linearly through the analysis; the fractional error in the area measurement translates directly to the uncertainty in the calculated cell thickness (t) and subsequently to the string defect density (ρ). Consequently, the system exhibits a uniform error propagation described by the relationship:

$$\frac{dA}{A} = \frac{dt}{t} = \frac{d\rho}{\rho} \approx 0.05$$

Further, the pixel-to-length calibration was established by equating a physical length of 80 mm to 1174 pixels. The precision of this calibration is limited by the finite thickness of the scale notation bars, which exhibit a standard deviation width of approximately 1.8 pixels. Accounting for the measurement uncertainty at both endpoints of the scale, the total pixel error accumulates to ≈ 3.6 pixels. Consequently, the relative error in the calibration factor(C) is estimated as:

$$\frac{\delta C}{C} = \frac{\delta L_{px}}{L_{px}} = \frac{3.6}{1174} \approx 0.3\%$$

This calibration uncertainty propagates to the string density calculation. Since the calculated cell volume (V) scales with the square of the calibration factor ($V \propto C^2$) while the measured string length scales linearly ($L \propto C$), the defect density depends inversely on the calibration factor ($\rho \propto C^{-1}$). Consequently, the magnitude of the relative error in density is equivalent to that of the calibration factor:

$$\frac{d\rho}{\rho} \approx \frac{dC}{C} \approx 0.3\%$$

This results in a total systematic uncertainty of 5.3% in the estimated string density.

Random error: To quantify the random error inherent in the experimental setup, five (three in the case of defect formation study) independent measurements were conducted on the same sample under identical conditions. The observed variations in the measured values are attributed to stochastic fluctuations in the detection mechanism and manual selection processes. These datasets were analyzed to compute the arithmetic mean (\bar{x}) and the standard deviation (σ), which serves as the primary metric for the random uncertainty. The final experimental result is reported as the mean with the standard deviation representing the measurement precision:

$$x = \bar{x} \pm \sigma = \frac{1}{N} \sum_{i=1}^N x_i \pm \sqrt{\frac{\sum_{i=1}^N (x_i - \bar{x})^2}{N-1}}$$

where $N = 5$ represents the number of trials. This statistical variation captures the reproducibility of the system, distinct from the systematic calibration errors discussed previously.

Prior to analysis, the three independent measurement series were time-shifted to align with a common temporal reference point ($t = 0$). To ensure the robustness of the subsequent model fitting, the dataset was filtered to exclude regimes of high variability. Specifically, the analysis interval was restricted to the range where the 20-point median value of relative standard deviation remained below **10%** of the mean value:

$$\text{Median} \left(\frac{\sigma(t_{-10})}{\bar{x}(t_{-10})}, \frac{\sigma(t_{-9})}{\bar{x}(t_{-9})}, \dots, \frac{\sigma(t_0 = t)}{\bar{x}(t_0 = t)}, \dots, \frac{\sigma(t_9)}{\bar{x}(t_9)} \right) (t) < \mathbf{0.1}$$

This criterion is introduced to suppress spurious fluctuations and to retain the underlying median trend of the data. Data points that violate this stability condition are discarded to ensure that transient deviations do not bias the extracted scaling parameters.

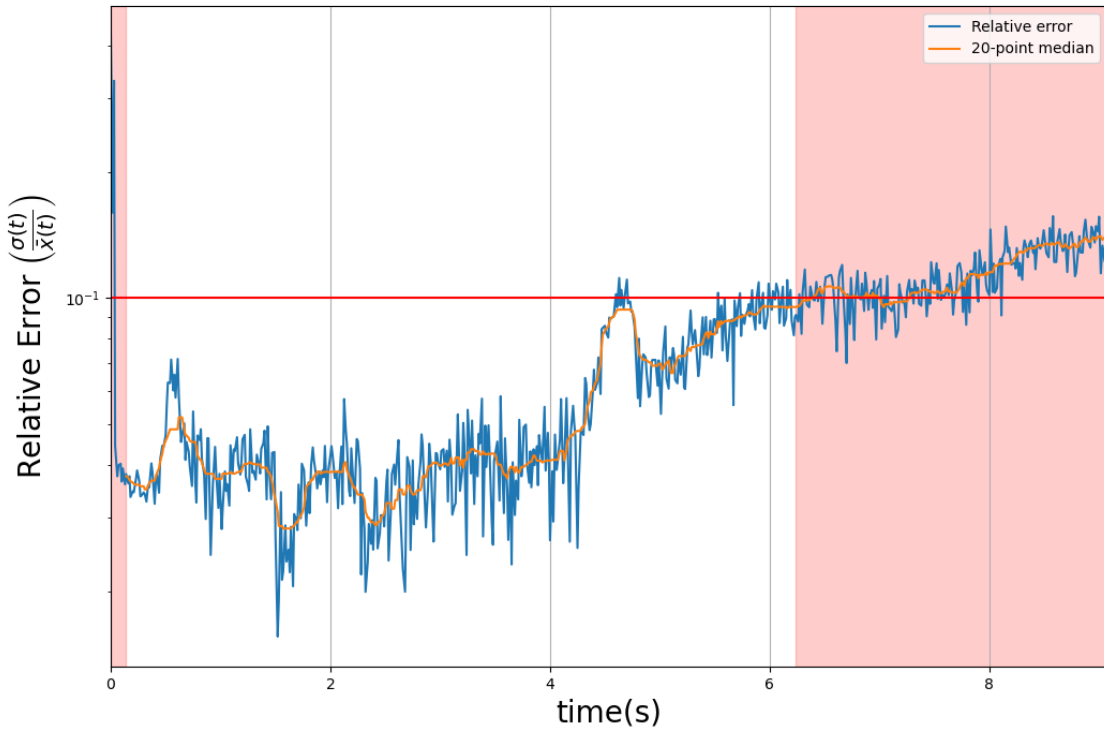


Figure 15: This example figure(60V data) shows the region selected based on the criteria given below. The shaded red regions mark data excluded from the analysis: early-time data (left) were discarded to remove the initial 10 frames, while the late-time tail (right) was excluded based on relative error selection criteria.

5 Conclusion

This project developed a reliable experimental and computational approach to study defect dynamics in nematic liquid crystals as a laboratory model for cosmological phase transitions. Although a direct experimental test of the Kibble–Zurek mechanism (KZM) scaling laws was not possible with the present setup, the work provided important insight into late-time defect evolution and the influence of topology and electric fields on nonequilibrium behavior.

In the late-time regime, a clear change in scaling behavior was observed, determined by the structure of the defect network. When permanent nucleation sites were present, the system evolved mainly through the annihilation of open line defects, and the defect density decayed as $\rho(t) \propto t^{-1}$, in agreement with standard one-scale coarsening theory. In contrast, in defect-free cells the system initially formed closed defect loops. Under strong electric fields, these loops were long-lived and decayed much more slowly than expected from simple tension-driven models. Additionally, variations in the π -wall width were observed during these dynamics, consistent with the expected influence of the electric field on the coherence length.

Efforts to study KZM scaling during defect formation showed that the experiment is limited by two extreme regimes. At high driving frequencies (10 kHz), the electric field changes too quickly for the liquid crystal molecules to respond, causing the system to freeze before

critical dynamics can develop. At lower frequencies, where molecular relaxation is possible, ion motion generates strong fluid flow that disrupts the ordered defect patterns. Because of this, no stable intermediate frequency range exists in the present sample configuration where the predicted KZM defect-scaling laws can be clearly observed.

Overall, these results demonstrate the robustness of late-time coarsening behavior in nematic liquid crystals while revealing practical limits imposed by material response times and electrohydrodynamic effects. Future studies could overcome these limitations by employing magnetic field quenches or rapid temperature quenches with suitable nematic materials to access universal defect-formation scaling. Furthermore, the observation of variable π -wall widths opens the door to quantitatively testing the inverse scaling of width with applied field strength, as predicted in literature [15]. Finally, the complex annihilation dynamics of umbilic defects, specifically their predicted S-shaped trajectories, could be resolved with much greater precision by applying sophisticated machine learning approaches to defect tracking [16].

A Acknowledgements

I would like to express my sincere gratitude to Prof. Pramoda for providing me with the opportunity to conduct this research in his laboratory. I am also deeply thankful to Ankit for his invaluable mentorship and unwavering support throughout the study.

I extend my gratitude to Prof. Somak and my SRC members for encouraging me to pursue this semester-long project and for granting me the academic autonomy to explore these ideas.

I also wish to thank Shri Gowri, Kurshid da, and all other members of our small physics family for the fruitful discussions and for helping me gain conceptual clarity. Their willingness to assist whenever I needed help was essential to the completion of this project.

I gratefully acknowledge the Departments of Chemistry and Biology for providing access to their laboratory facilities.

Finally, I would like to acknowledge the developers of the open-source software ImageJ and other scientific analysis tools (e.g. scikit-image) that significantly streamlined this work. Specifically, I thank the creators of GitHub for managing project repositories, Overleaf for the seamless typesetting environment, and Mendeley for bibliography management. I also appreciate the utility of generative artificial intelligence tools, particularly for their artificial intelligence-assisted search prompts, which accelerated the literature review and documentation process.

References

- [1] Kibble, T. W. Topology of cosmic domains and strings. *Journal of Physics A: Mathematical and General* **9**, 1387 (1976). URL <https://iopscience.iop.org/article/10.1088/0305-4470/9/8/029>.
- [2] Centre for Theoretical Cosmology: The Origins of the Universe: Phase transitions. URL https://www.ctc.cam.ac.uk/outreach/origins/cosmic_structures_one.php.
- [3] Early Universe Cosmology and Tests of Fundamental Physics - A. Albrecht et al. URL https://ned.ipac.caltech.edu/level5/Sept01/Albrecht/Albrecht_contents.html.

- [4] Kibble, T. W. B. Phase Transitions in the Early Universe. *Acta Phys. Polon. B* **13**, 723 (1982). URL <https://www.actaphys.uj.edu.pl/R/13/10/723>.
- [5] Vilenkin, A. Cosmic strings and domain walls. *Physics Reports* **121**, 263–315 (1985). URL <https://www.sciencedirect.com/science/article/abs/pii/037015738590033X>.
- [6] Centre for Theoretical Cosmology: The Origins of the Universe: Cosmic strings and other cosmological defects. URL https://www.ctc.cam.ac.uk/outreach/origins/cosmic_structures_two.php.
- [7] Shellard, E. P. & Brandenberger, R. H. Clusters of galaxies from cosmic strings. *Physical Review D* **38**, 3610 (1988). URL <https://journals.aps.org/prd/abstract/10.1103/PhysRevD.38.3610>.
- [8] Kibble, T. Phase-transition dynamics in the lab and the universe. *Physics Today* **60**, 47–52 (2007). URL <https://doi.org/10.1063/1.2784684>.
- [9] Zurek, W. H. Cosmological experiments in superfluid helium? *Nature* **317**, 505–508 (1985). URL <https://www.nature.com/articles/317505a0>.
- [10] Zurek, W. H. Cosmological experiments in condensed matter systems. *Physics Reports* **276**, 177–221 (1996). URL <https://www.sciencedirect.com/science/article/abs/pii/S0370157396000099?via%3Dihub>.
- [11] Chuang, I., Durrer, R., Turok, N. & Yurke, B. Cosmology in the Laboratory: Defect Dynamics in Liquid Crystals. *Science* **251**, 1336–1342 (1991). URL <https://doi.org/10.1126/science.251.4999.1336>.
- [12] Chuang, I., Turok, N. & Yurke, B. Late-time coarsening dynamics in a nematic liquid crystal. *Physical Review Letters* **66**, 2472 (1991). URL <https://journals.aps.org/prl/abstract/10.1103/PhysRevLett.66.2472>.
- [13] Yurke, B., Pargellis, A. N., Chuang, I. & Turok, N. Coarsening dynamics in nematic liquid crystals. *Physica B: Condensed Matter* **178**, 56–72 (1992). URL <https://www.sciencedirect.com/science/article/abs/pii/092145269290179V>.
- [14] Shen, Y. & Dierking, I. Annihilation dynamics of reverse tilt domains in nematic liquid crystals. *Journal of Molecular Liquids* **313**, 113547 (2020). URL <https://www.sciencedirect.com/science/article/abs/pii/S016773222033021X>.
- [15] Blanc, C., Svenšek, D., Žumer, S. & Nobili, M. Dynamics of Nematic Liquid Crystal Disclinations: The Role of the Backflow. *Physical Review Letters* **95**, 097802 (2005). URL <https://journals.aps.org/prl/abstract/10.1103/PhysRevLett.95.097802>.
- [16] Dierking, I. *et al.* Machine Learning Analysis of Umbilic Defect Annihilation in Nematic Liquid Crystals in the Presence of Nanoparticles. *Crystals* **2025**, Vol. 15, Page 214 **15**, 214 (2025). URL <https://www.mdpi.com/2073-4352/15/3/214>.
- [17] Gennes, P. G. D. & Prost, J. The Physics of Liquid Crystals. *The Physics of Liquid Crystals* (1993). URL <https://academic.oup.com/book/54859>.

- [18] Palffy-Muhoray, P. The diverse world of liquid crystals. *Physics Today* **60**, 54–60 (2007). URL <https://doi.org/10.1063/1.2784685>.
- [19] Fowler, N. & Dierking, D. I. Kibble–Zurek Scaling during Defect Formation in a Nematic Liquid Crystal. *ChemPhysChem* **18**, 812–816 (2017). URL <https://doi.org/10.1002/cphc.201700023>.
- [20] Van Der Walt, S. *et al.* Scikit-image: Image processing in python. *PeerJ* **2014** (2014). URL <https://scikit-image.org/>.
- [21] Meijering, E. *et al.* Design and Validation of a Tool for Neurite Tracing and Analysis in Fluorescence Microscopy Images. *Cytometry Part A* **58**, 167–176 (2004). URL <https://doi.org/10.1002/cyto.a.20022>.
- [22] Canny, J. A Computational Approach to Edge Detection. *IEEE Transactions on Pattern Analysis and Machine Intelligence* **PAMI-8**, 679–698 (1986). URL <https://ieeexplore.ieee.org/document/4767851>.
- [23] Skeleton analysis with Skan — Skan 0.13.0. URL <https://skeleton-analysis.org/stable/>.

B Late-time coarsening

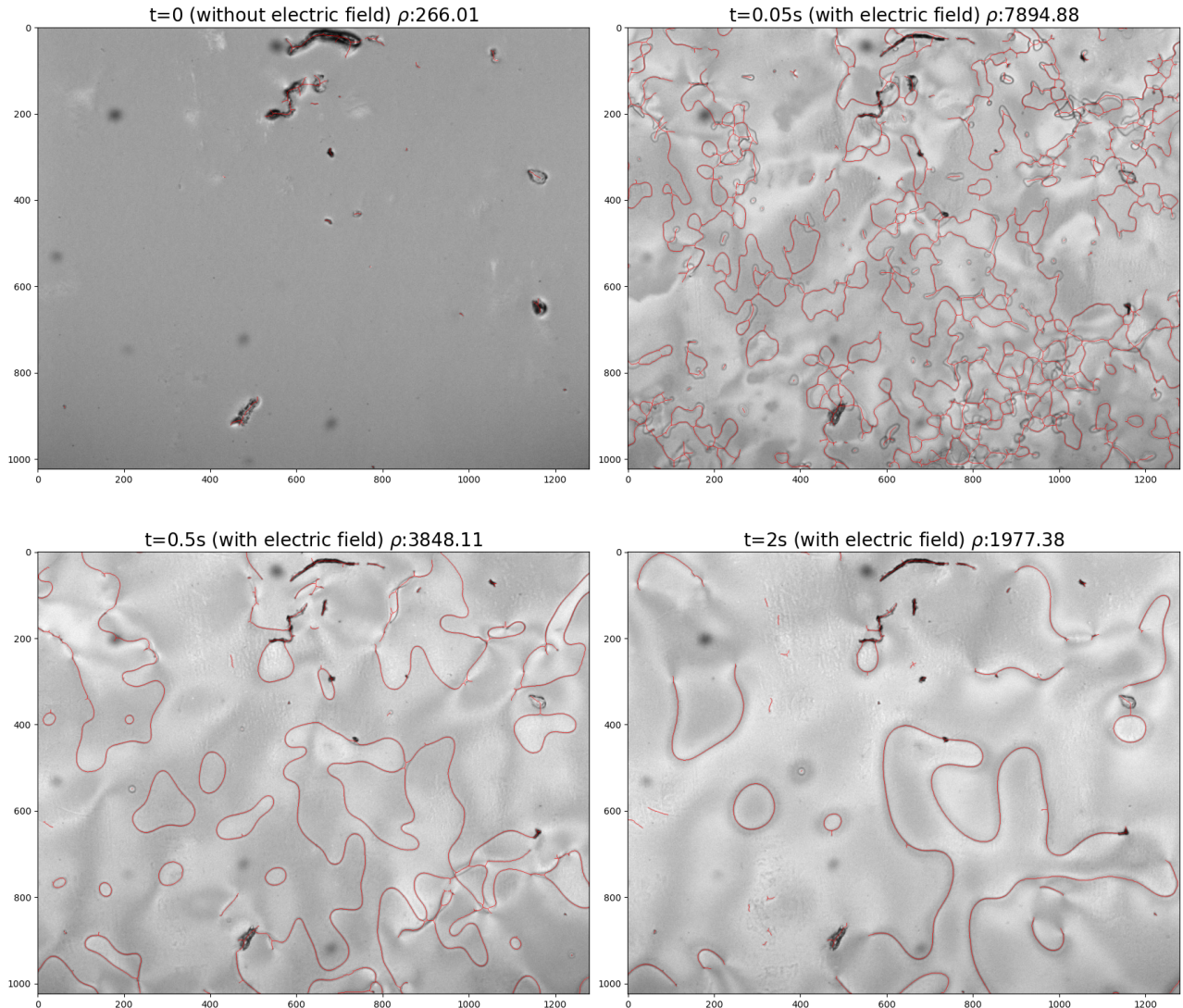


Figure 16: Topological defects at different time stamps for 60V 10× (Old liquid crystal cell of thickness $31.09 \pm 0.44\mu m$ with permanent defect points). Red curves are the defect lines detected by the implemented framework.

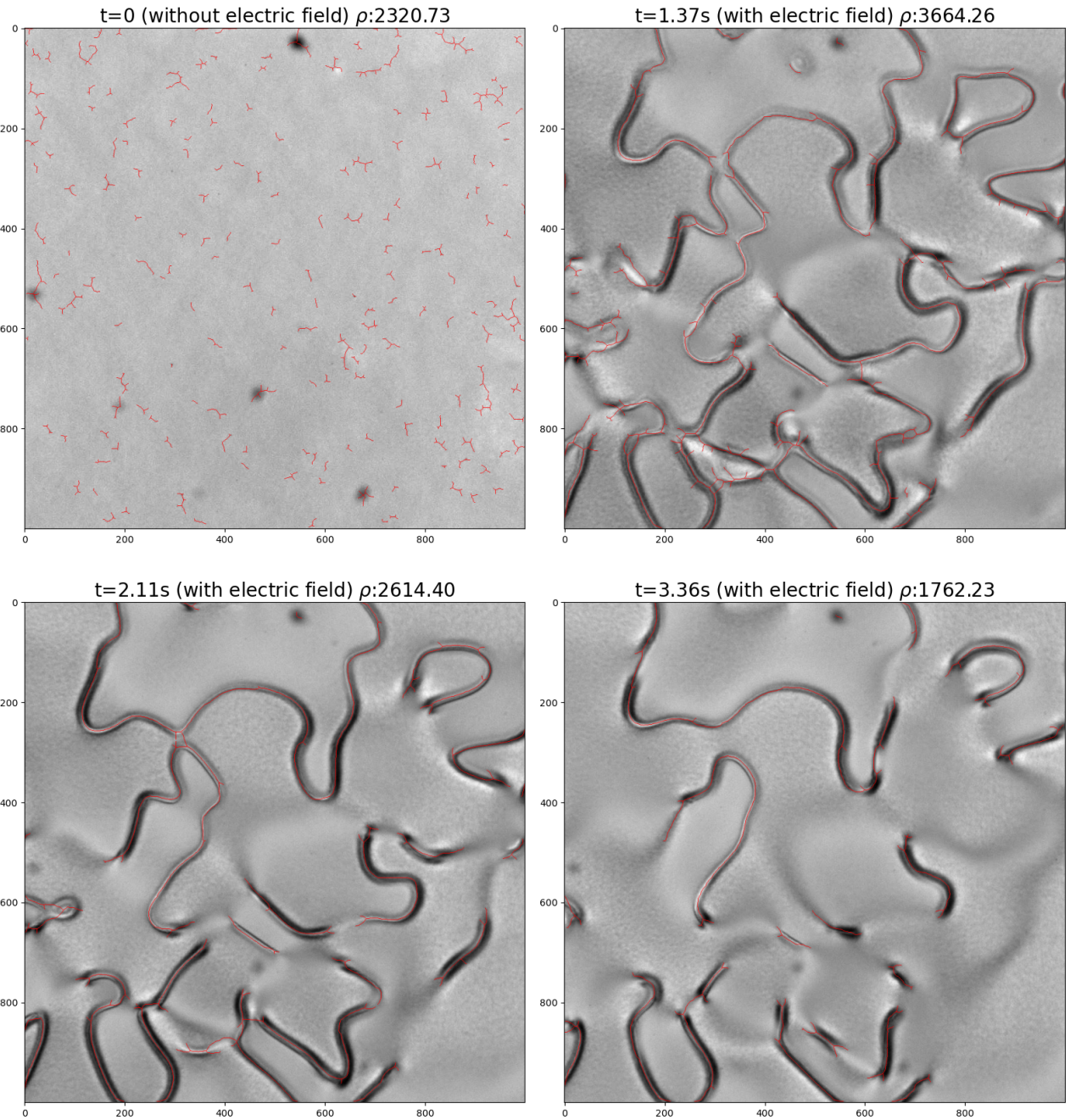


Figure 17: Topological defects at different time stamps for 10V $10\times$. Red curves are the defect lines detected by the implemented framework.

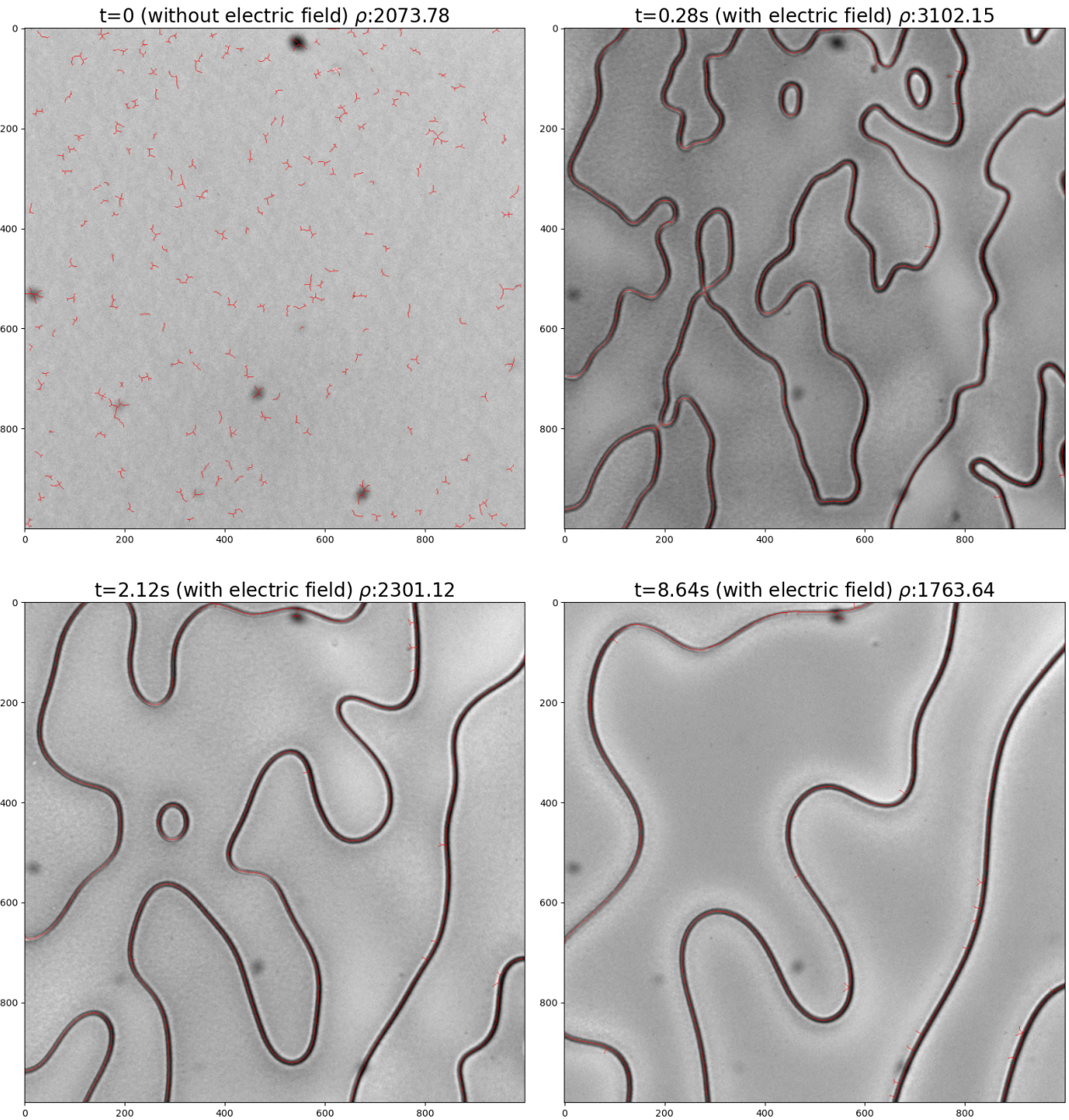


Figure 18: Topological defects at different time stamps for 20V 10 \times . Red curves are the defect lines detected by the implemented framework.

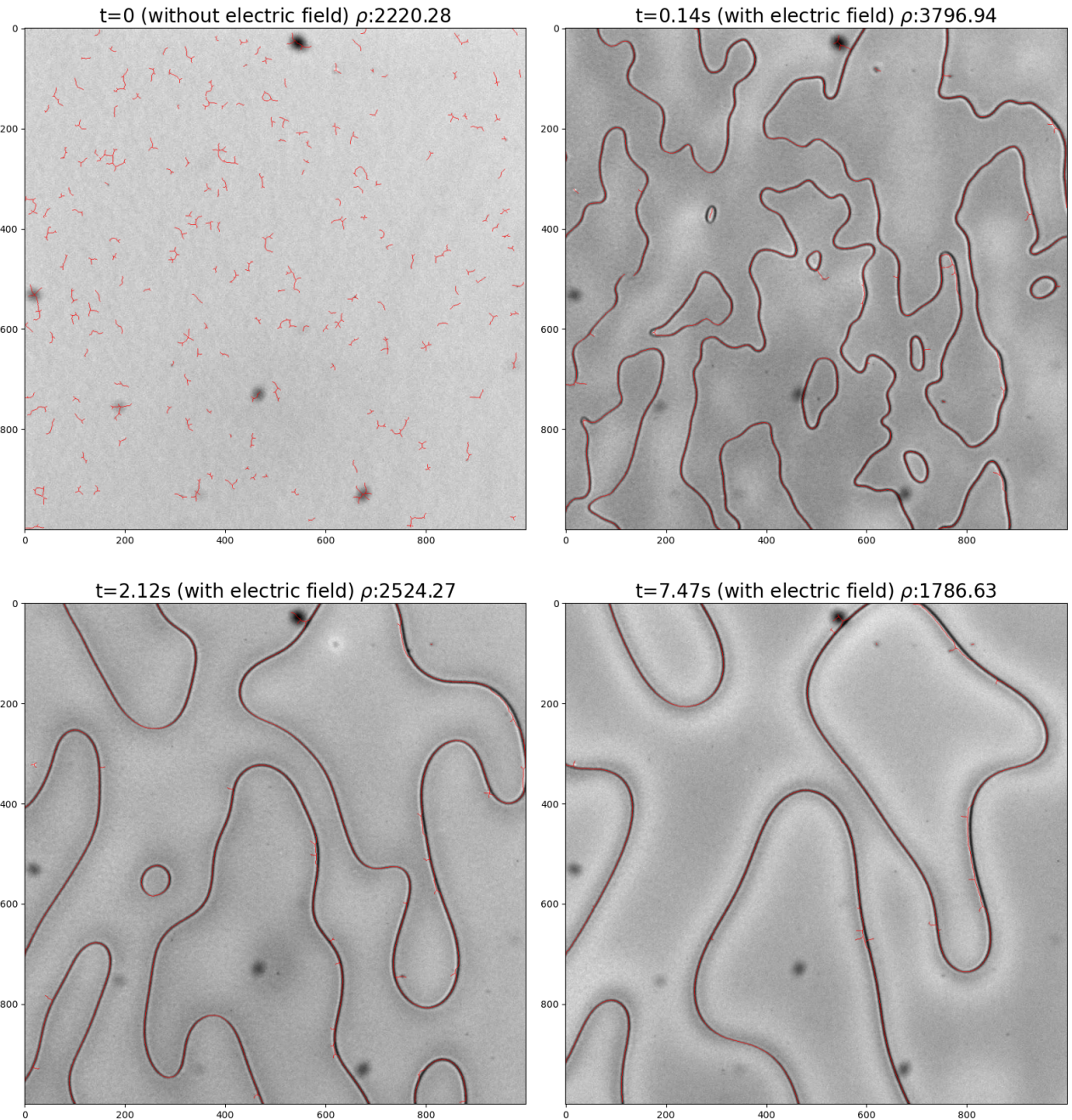


Figure 19: Topological defects at different time stamps for 40V 10 \times . Red curves are the defect lines detected by the implemented framework.

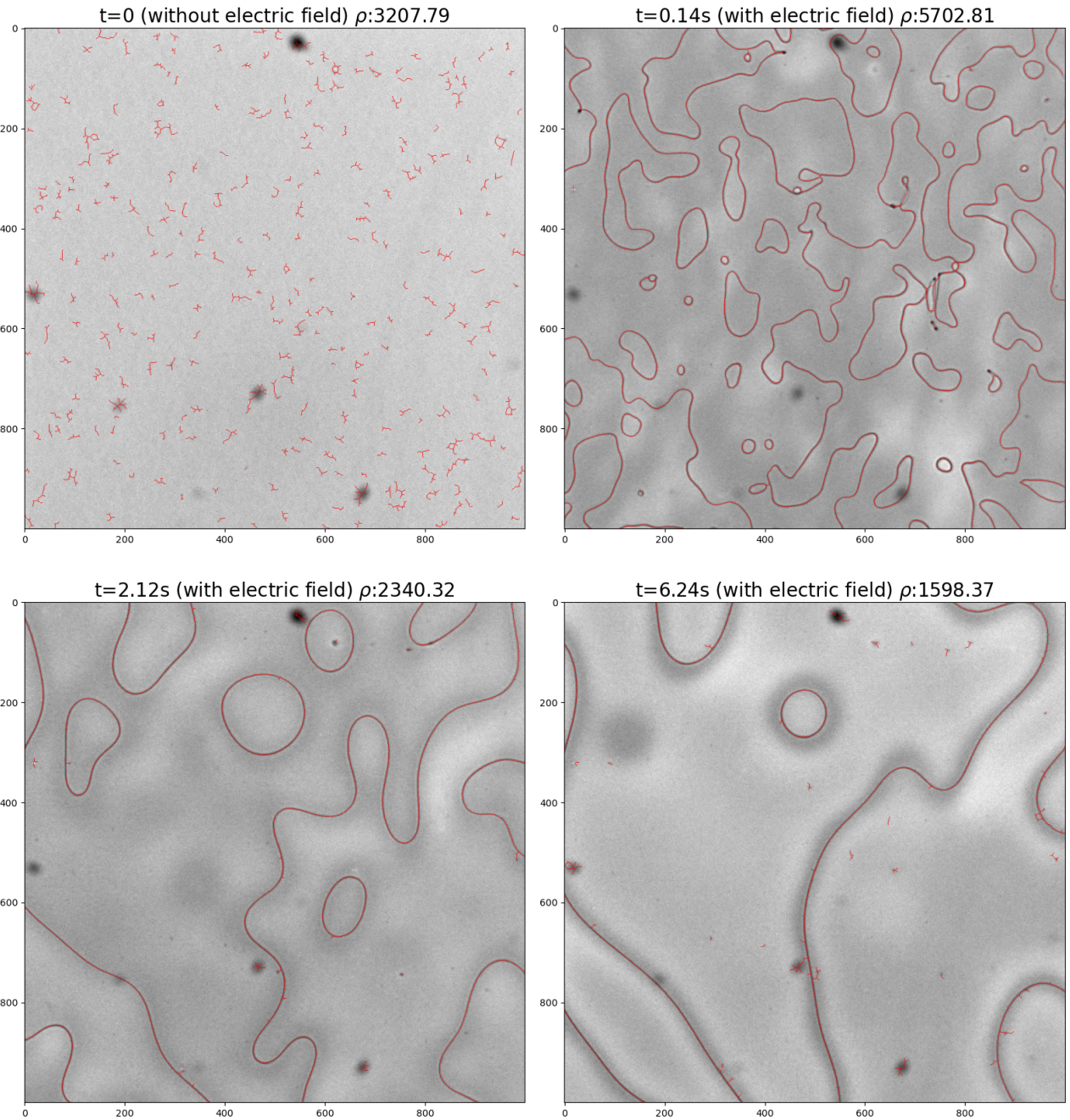


Figure 20: Topological defects at different time stamps for 60V 10 \times . Red curves are the defect lines detected by the implemented framework.